PHYSICAL REVIEW E VOLUME 59, NUMBER 1 JANUARY 1999

Simulation of a two-dimensional shear cell

Steffen Schöllmann
Solitudeallee 82, 70825 Korntal-Münchingen, Germany

(Received 5 August 1998)

Molecular dynamics (MD) simulations of a two-dimensional (2D) shear cell of Couette type are presented. The simulation is adjusted to corresponding experimental studies and the results are compared with the experimental results of model granulate consisting of about 3000 photoelastic disks. A shear zone next to the rotating inner wall is observed. The distribution of tangential velocity of the disks shows an exponential decrease within the shear zone and the angular velocities of the disks oscillate in the shear zone. The probability distributions of the fluctuational tangential, radial, and angular velocities of the disks become narrower with increasing distance from the inner boundary and are non-Gaussian with exponential flanks. We find a comparatively weak influence of both, the restitution coefficient, and the friction coefficient, on the tangential velocity profile, whereas the packing fraction crucially determines the system's response. The contact network of the disk packing reveals force chains. The mean fabric tensor for each disk shows a different behavior within and outside the shear zone. The probability distribution of normal contact forces shows an exponential decay for high forces. [S1063-651X(99)12301-8]

PACS number(s): 83.50.Ax, 83.20.Jp, 83.10.Hh, 83.70.Fn

I. INTRODUCTION

For several decades, granular media such as sand, gravel, powder, or pills were a research topic almost only in the engineering community [1]. In recent years, physicists have become more and more interested in granular media [2–4]. A lot of experimental and theoretical work was and still is carried out [5,6,3]. Whereas engineers frequently use continuum models to describe the behavior of granular materials, a discrete view is also possible. Using well known simulation methods like Monte Carlo (MC) and molecular dynamics (MD) simulations [7], such different effects as size segregation [8–10], convection [11,12] or pattern formation [13–15] can be studied. Simple shear flow of granulates has also been explored using discrete simulations [16–19].

Different types of shear cells have been studied [20–22]. These studies are often performed using ''real'' granular materials such as sand or soils and are focused on topics important for industrial applications. But, since detailed insights into the microscopic behavior of these materials is hard to achieve, the use of ''model granulates'' consisting of rather small numbers of idealized grains such as spheres or disks is recommended. Experimental studies of the dynamics within a shear cell focus on force fluctuations and stress distributions [23–25].

Here, we focus on molecular dynamics (MD) simulations of a two-dimensional (2D) cylindrical shear cell, as also examined experimentally [26]. The experimental shear cell consists of an inner ring that rotates with a variable angular velocity and a fixed outer ring, both confining about 3000 disks in the gap. The disks are made of photoelastic material and the top and bottom plates are transparent with crossed polarizers to visualize stresses [26]—one aim is to get agreement with the experimental results. Furthermore, we make some predictions on the distribution of contact forces. We describe the simulation method in Sec. II, and the shear cell setup in Sec. III. Parameter studies and results concerning the kinematics will be presented in Sec. IV. In Sec. V contacts and forces within the granular packing will be investigated. A discussion and outlook follow in Sec. VI.

II. SIMULATION METHOD

We use a discrete MD simulation method [27,7], i.e., we integrate the equations of motion for each particle. Therefore, the force $\vec{f}_i(t)$ on particle i at time t is needed to calculate the acceleration. In general, $\vec{f}_i$ consists of a force $\vec{f}_i^{\mathrm{ex}}$ due to an external field as gravitation, and pair interaction forces $\vec{f}_{ij}$ exerted by another particle j on particle i. In our simulation, the particles experience no external field and $\vec{f}_{ij}$ is a contact interaction and thus of short range. The force $\vec{f}_{ij}$ is divided into two components: a force $\vec{f}_{ij}^{(\mathrm{n})}$ normal to the contact plane between two disks and $\vec{f}_{ij}^{(\mathrm{t})}$ parallel to the contact plane. For $\vec{f}_{ij}^{(\mathrm{n})}$ we use a linear spring-dashpot model consisting of two components. First, a linear elastic repulsion force

$$\vec{f}_{ij}^{(\mathrm{el})}=k_{\mathrm{n}}y_{ij}\vec{n}_{ij} \tag{1}$$

with the overlap $y_{ij}=r_{ij}-\frac{1}{2}(d_i+d_j)$ of particles i and j, the spring constant k_{n} and normal unit vector $\vec{n}_{ij}=(\vec{r}_j-\vec{r}_i)/r_{ij}$ pointing from particle i to particle j. The distance between the centers of the particles i and j with positions $\vec{r}_i$ and $\vec{r}_j$ is $r_{ij}=|\vec{r}_i-\vec{r}_j|$ and $d_i(d_j)$ is the diameter of particle $i(j)$. Second, we use a viscous damping force

$$\vec{f}_{ij}^{(\mathrm{diss})}=\gamma_{\mathrm{n}}(\vec{v}_{ij}\cdot\vec{n}_{ij})\vec{n}_{ij}\,, \tag{2}$$

with the relative velocities $\vec{v}_{ij}=\vec{v}_j-\vec{v}_i$ of particles i and j and a phenomenological viscosity γ_{n}. For high values of the viscosity γ_{n} the normal force $\vec{f}_{ij}^{(\mathrm{n})}=\vec{f}_{ij}^{(\mathrm{el})}+\vec{f}_{ij}^{(\mathrm{diss})}$ is discontinuous at the beginning of the interaction and can become attractive at the end [28,29]. We avoid the latter numerical artifact by setting $\vec{f}_{ij}^{(\mathrm{n})}$ to zero if $\vec{f}_{ij}^{(\mathrm{n})} \cdot \vec{n}_{ij}$ would become positive and thus attractive.

The tangential component $\vec{f}_{ij}^{(\mathrm{t})}$ is the friction force between two disks in contact. Several types of friction forces can be found in literature [30]. Most simple is a Coulomb friction where $\vec{f}_{ij}^{(\mathrm{t})}$ is proportional to the normal force $\vec{f}_{ij}^{(\mathrm{n})}$:

$$\vec{f}_{ij}^{(\mathrm{t})} = -\mu |\vec{f}_{ij}^{(\mathrm{n})}| \vec{t}_{ij}, \tag{3}$$

with a friction coefficient μ and directed opposite to the unit vector in tangential direction $\vec{t}_{ij} = \vec{v}_{ij}^{(\mathrm{t})}/|\vec{v}_{ij}^{(\mathrm{t})}|$ and so antiparallel to the tangential velocity $\vec{v}_{ij}^{(\mathrm{t})} = \vec{v}_{ij} - (\vec{v}_{ij} \cdot \vec{n}_{ij})\vec{n}_{ij}$. Because of the discontinuity of $\vec{t}_{ij}$ at zero relative tangential velocities, the use of a regularized force law

$$\vec{f}_{ij}^{(\mathrm{t})} = -\min(|\gamma_{\mathrm{t}} \vec{v}_{ij}^{(\mathrm{t})}|, |\mu \vec{f}_{ij}^{(\mathrm{n})}|) \vec{t}_{ij}. \tag{4}$$

is recommended [30]. Here, γ_{t} may be considered as a technical parameter that should be large enough to avoid substantial differences to Eq. (3) and small enough to avoid the discontinuities mentioned above. However, the force in Eq. (4) is not able to model tangential elasticity, i.e., an inversion of tangential velocity during a contact, as measured experimentally [31,32].

To model tangential elasticity and static friction, Cundall and Strack [27] proposed the use of a tangential spring between two disks in contact:

$$\vec{f}_{ij}^{(\mathrm{t})} = -\min\left(k_{\mathrm{t}} \vec{\zeta}_{ij}, \frac{|\mu \vec{f}_{ij}^{(\mathrm{n})}|}{|\vec{\zeta}_{ij}|} \vec{\zeta}_{ij} \right), \tag{5}$$

where k_{t} is the tangential stiffness and $\vec{\zeta}_{ij}$ denotes the elongation of the spring since time t_0 when the contact was established:

$$\vec{\zeta}_{ij}(t) = \int_{t_0}^{t} \vec{v}_{ij}^{(\mathrm{t})}(t')\,\mathrm{d}t'. \tag{6}$$

Let us point out that Eq. (5) is *not* just the minimum of the spring force in Eq. (6) and the Coulomb force in Eq. (3). The Coulomb force in Eq. (5) can have a different direction than in Eq. (3) since it is coupled to the direction of the spring elongation $\vec{\zeta}_{ij}$ rather than to the direction of relative velocity $\vec{t}_{ij}$. For more details on modeling the tangential force see [30].

Recently, the question came up as to whether Eq. (5) is the correct implementation or not [33,29]. Different ways of implementation were tested with the conclusion that either the viscous force law in Eq. (4) or a special implementation of Eq. (5) should be used. The latter includes that the spring is kept at a length that resembles a fully activated frictional contact. This is in contrast to the model where the spring is released or cut when the force exceeds the Coulomb limit. Illustratively speaking, the spring has to be dragged. However, a comparison of the different implementations did not yield different results.

Finally, we will introduce a friction force F_{bottom} between a disk and the bottom plate:

$$\vec{F}_{\mathrm{bottom}} = -\mu_{\mathrm{bottom}} |\vec{G}_{\mathrm{disk}}| \frac{\vec{v}_i}{|\vec{v}_i|}. \tag{7}$$

G_{disk} is the weight of one disk and μ_{bottom} is the friction coefficient between disks and bottom plate. $\vec{F}_{\mathrm{bottom}}$ is oriented in the opposite direction of the momentary velocity $\vec{v}_i$ of disk i.

The linear elastic repulsion of Eq. (1) together with the viscous damping of Eq. (2) constitute a damped harmonic oscillator whose motion can be solved analytically. The typical contact duration for small γ is found to be $t_{\mathrm{c}} = \pi/\omega$, with the damped frequency $\omega = \sqrt{\omega_0^2 - \overline{\gamma}^2}$, the frequency $\omega_0 = \sqrt{k_{\mathrm{n}}/m_{ij}}$ for $\gamma_{\mathrm{n}} = 0$, the scaled viscosity $\overline{\gamma} = \gamma_{\mathrm{n}}/(2m_{ij})$, and the reduced mass $m_{ij} = m_i m_j/(m_i + m_j)$. The coefficient of normal restitution e_{n} is defined as the ratio of the normal velocities after and before contact $e_{\mathrm{n}} = -v^{(\mathrm{n})}(t_{\mathrm{c}})/v^{(\mathrm{n})}(0)$ and can be calculated as $e_{\mathrm{n}} = \exp(-\pi\overline{\gamma}/\omega)$. Note that t_c and e_{n} are strictly valid for small $\overline{\gamma}$ only, since we use the condition $\vec{f}_{ij}\vec{n}_{ij} > 0$ to determine when a contact ends. For a more detailed calculation see Ref. [34]. Technically, in MD simulations one has to ensure that the integration time step t_{MD} is small compared to the contact duration t_{c}, in order to have the integration algorithm working well. To get good energy conservation for $\gamma_{\mathrm{n}} = 0$, the ratio $t_{\mathrm{c}}/t_{\mathrm{MD}}$ must not be smaller than about 40. We compared several integration schemes and present here results obtained with the Verlet method using $t_{\mathrm{c}}/t_{\mathrm{MD}} = 60$. There are several techniques known to reduce time and memory consumption of MD simulations [7]. In the simulations presented here, we use Verlet neighborhood tables, since the neighborhood is changing rather slowly.

The stiffness k_{n} is a function of the Young modulus Y and the Poisson ratio ν of the material. According to the Hertz theory [35], a more complicated dependence of k_{n} on the impact velocity and the overlap is found for spheres, e.g., $k_{\mathrm{n}} \propto \sqrt{y}$ with the overlap y. For disks a linear dependence of k_{n} on the overlap y is found [36]. We use for all simulations the linear spring model according to Eqs. (1) and 2 because we have disks, not spheres. Furthermore, the linear spring model is easier to handle numerically than the nonlinear Hertz model and the normal interaction during a contact is supposed to be less important than the tangential friction in the shear cell [37]. Thus, we use for all simulations the linear spring-dashpot model according to Eqs. (1) and 2.

The two parameters k_{n} and γ_{n} can be determined by applying two criteria: first, the spring constant k_{n} can be directly derived from the Young modulus Y of the material. Second, the restitution coefficient used should be of the same order of magnitude as the one measured.

III. SIMULATION SETUP

The geometrical setup of the shear cell is shown in Fig. 1. The radii of the inner and the outer ring are $r^{(\mathrm{in})} = 10.32$ cm and $r^{(\mathrm{out})} = 25.24$ cm, respectively. The inner ring is rotating with a typical angular velocity $\omega^{(\mathrm{in})} = 0.1\ \mathrm{s}^{-1}$ while the outer ring is immobile. Thus, one revolution takes approximately 1 m. Typically one observes a shear zone of several particle diameters thickness close to the inner ring. It is also possible to rotate the outer ring instead

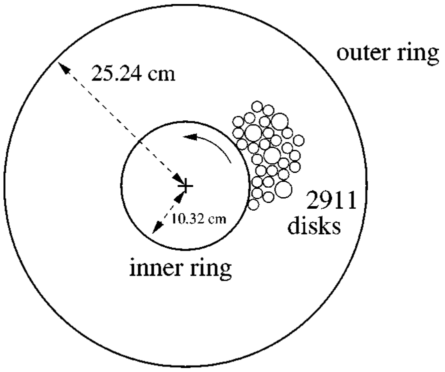

FIG. 1. Schematic picture of the 2D shear cell.

of the inner one. In the experiment the rings are approximately 6 mm high and the system is confined in the plane by transparent plexiglass plates. For an enlarged sketch of the surfaces of the rings used in the experiment, see Fig. 2(a). We implement these walls as shown in Fig. 2(b). It is more convenient to simulate the wall surface by a smooth cylindrical wall overlapped with disks as shown in Fig. 2(b) than to simulate the exact polygonal experimental boundary [38]. This difference between experiment and simulation should not influence the results remarkably. If not explicitly mentioned, we use 2911 disks with two different diameters: 2511 small disks with diameter $d^{(\mathrm{small})}=7.42$ mm and 400 larger disks with $d^{(\mathrm{large})}=8.99$ mm. The height h of all disks is 6 mm, in the experiment. In the simulations, however, we neglect the third dimension, as far as the size of the particles is concerned, and assume the system to be infinitely long. The volume fraction ρ of this configuration is 0.811. The material properties of the disks are given in Table I. For the friction law of Eq. (4) we use the experimentally determined value of μ and choose γ_{t} to be 0.15. We adjusted the parameters $k_{\mathrm{n}}=352.1$ N/m and $\gamma_{\mathrm{n}}=0.19$ kg/s so that t_c and e_{n} take the values measured experimentally. The parameters of the simulations are given in Table II. To get an initial shear cell setup, we put the desired number of disks on a triangular lattice with spacing $a=d^{(\mathrm{large})}$ [as shown in Fig. 3(a)], give them random initial velocities and compress the system, i.e., we reduce the radius of the outer ring until it reaches the selected value $r^{(\mathrm{out})}$. The system after compression is shown in Fig. 3(b). First, we checked different random sequences of the small and large disks on the lattice and found no influence on the behavior of the packing during shearing. Second we varied the initial lattice spacing a, also without a detectable effect on the global behavior of the system. However, we recognized that the system remembers its initial regular packing after the compression if the lattice spacing is too small. Only for a lattice spacing of $a=5d^{(\mathrm{large})}$ we found no more indication of the initial regularity after compression. Since we could not detect an influence of a on the system behavior, we use $a=d^{(\mathrm{large})}$ in the following.

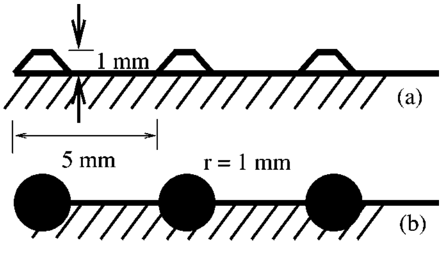

FIG. 2. Surface of rings in the experiment (a) and in the simulation (b).

TABLE I. Experimentally determined material parameters.

Density $\overline{\rho}$	1.06 g cm^{-3}
Young modulus $\underline{Y}$	4.8 MPa
Poisson ratio ν	0.5
Restitution coefficient e_{n}	0.3
Friction coefficient μ	0.44

IV. PARAMETER STUDIES AND KINEMATICS

The first task is to check the agreement with the experiment. As one criterion for agreement we use the tangential velocity profile, i.e., the mean tangential velocity v_{t}' of disks as a function of the radial distance from the center. We normalize the tangential velocity $v_{\mathrm{t}}=v_{\mathrm{t}}'/(\omega^{(\mathrm{in})}r')$ and the radial position $r=(r'-r^{(\mathrm{in})})/d^{(\mathrm{small})}$. Thus, $v_{\mathrm{t}}=1$ means that a disk follows the rotation of the inner ring, like a solid object, and r measures the distance *from* the inner ring in units of disk diameters.

In order to get a mean tangential velocity at a certain radius r we perform temporal and spatial averaging. First, we average over a number n^{t} of snapshots of the shear cell separated by time intervals Δt. Second, we average over all disks at a radial position r' with $r'\in[r-\Delta r/2, r+\Delta r/2]$, where Δr is determined by the total number n^{r} of radial positions used for the statistics. For the results presented in this paper we use $n^{\mathrm{t}}=300$, $\Delta t=0.2$ s, $n^{\mathrm{r}}=50$, and $\Delta r=1.5$ mm if not explicitly mentioned.

At the beginning of the shearing, the system passes a transition from the initial configuration to a steady state with a stationary shearing of the granulate and thus a time-independent tangential velocity profile. Our simulation shows that this transient period happens during the first revolution of the inner wheel. After two revolutions we could not recognize any systematic change in the averaged quantities. However, since we simulated only a maximum of 10 revolutions a long-time change cannot be excluded from our results. The following results are obtained during the second revolution of the cell.

TABLE II. Parameters used for a typical simulation.

Density $\overline{\rho}$	1.06 g cm^{-3}
Normal spring constant k_{n}	352.1 N/m
Normal viscosity γ_{n}	0.19 kg/s
Restitution coefficient e_{n}	0.3
Friction coefficient μ	0.44
Tangential viscosity γ_{t}	0.15 kg/s
Contact duration t_{c}	2.4×10^{-3} s
Time discretization t_{MD}	4×10^{-5} s
Tangential spring constant k_{t}	0 N/m
Bottom friction μ_{bottom}	2×10^{-5}

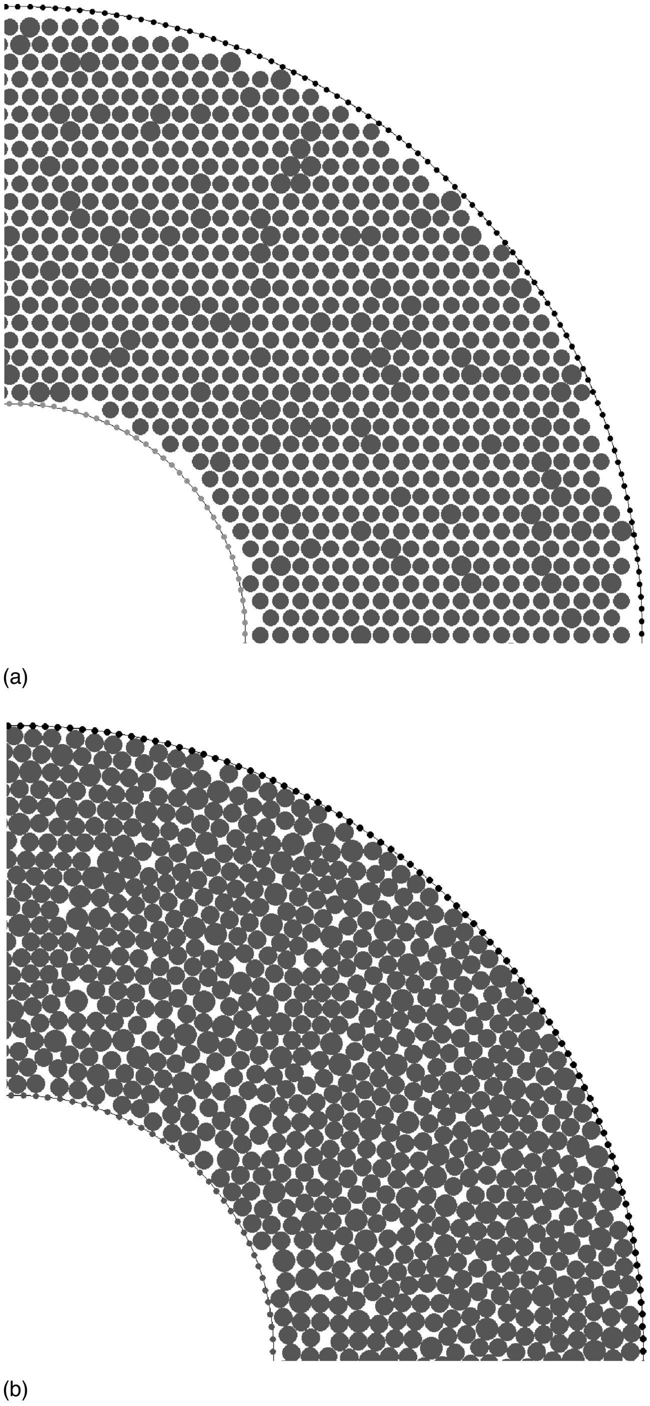

FIG. 3. (a) Initially, the disks are put on a triangular lattice with spacing $d^{(\mathrm{large})}$. (b) Shear cell after compression when the outer ring has reached the radius $r^{(\mathrm{out})}$.

A. Variation of the model parameters

In Fig. 4 we compare the tangential velocities measured in the simulation with those from the experiment. In the experiment, a strong decay of v_{t} from the inner ring outwards is observed. In the outer regions v_{t} is comparable to the noise level. We will refer to the area of the strong decay (within the innermost disk layers) as the *shear zone*. Note that $v_{\mathrm{t}} < 1$ close to the inner wall, indicating that an essential portion of the particles at the shear wall are sliding. The result of the simulation is qualitatively the same but the velocities are systematically too high. In the following, we study the influence of several parameters on the tangential velocity profile. Figure 5 shows that a higher friction coefficient μ leads to a larger tangential velocity in the shearing zone but to *smaller* velocities outside. The width of the shear-zone is not influenced much by μ, i.e., the curves in Fig. 5 cross at $r \approx 6$. There are two types of friction between the inner ring and the adjacent disks: first a ''microscopic'' friction that results from the Coulomb friction according to Eq. (3), and second, a ''macroscopic'' friction due to the surface roughness as shown in Fig. 2. Note that even with very low Coulomb friction ($\mu = 0.05$) a considerable shearing of the granulate takes place mostly due to the rough surface of the inner ring.

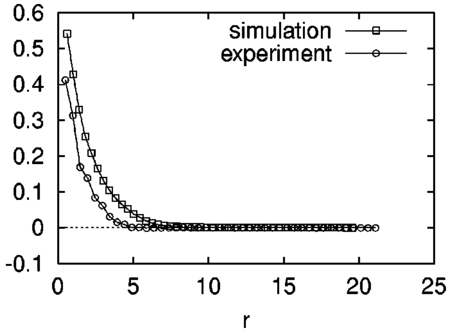

FIG. 4. Mean tangential velocity v_{t} as a function of the radius r.

In Fig. 6 we present tangential velocity profiles obtained from simulations with different restitution coefficients e_{n}. A weak dependence of the tangential velocity profile on the restitution coefficient e_{n} is found but no clear tendency can be evidenced. The data for $e_{\mathrm{n}} = 0.2$ and $e_{\mathrm{n}} = 0.8$ are almost indistinguishable, whereas the results for $e_{\mathrm{n}} = 0.6$ show slightly larger tangential velocities. This result indicates that the system is in a state where most of the kinetic energy is dissipated and the rate of energy dissipation in normal direction is not very important.

Especially in the outer area where the particles are almost at rest, the static friction between disks is supposed to play an important role. Therefore we use the friction law of Eq. (5) with tangential springs to model a kind of static friction between disks and also between disks and boundaries. We simulated two particle collisions as described in [30] to check the friction law, Eq. (5), and found that the influence of the tangential springs on the tangential velocity gets stronger with increasing $\alpha = k_{\mathrm{t}}/k_{\mathrm{n}}$. The value of $\alpha \approx 0.5$ leads to a reasonable agreement of the model with experiments [30].

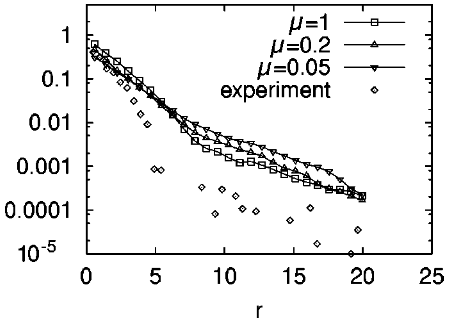

FIG. 5. Semilogarithmic plot of the mean tangential velocity v_{t} vs radius r for different friction coefficients μ.

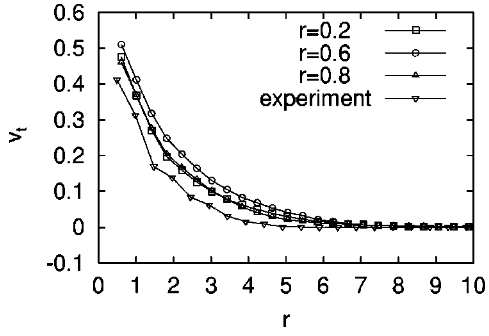

FIG. 6. Mean tangential velocity v_{t} vs radius $\underline{r}$ obtained from simulations with different restitution coefficients e_{n}. The Coulomb friction is $\mu=0.44$.

For $k_{\mathrm{n}}=352.1$ N/m, $\alpha=0.5$ yields a tangential stiffness $k_{\mathrm{t}}=176$ N/m; the stiffness k_{t} for a different value of α is being calculated correspondingly. Figure 7 shows that a different strength of the tangential spring k_{t} in Eq. (5) does not influence the shear zone, while we evidence a very small effect in the outer region. Since even different values of α do not produce remarkably different tangential velocities, we will use $\alpha=0$ in the following. We thus apply no static friction.

We were not able to achieve a reasonable agreement between experiments and simulations by changing the friction coefficient μ, the restitution coefficient e_{n}, or the tangential stiffness k_{t}. This rather unexpected result indeed rectifies the choice of an interaction model as simple as possible from the numerical viewpoint.

B. Friction with the walls

In the experiment, there is an additional friction between the disks and the bottom (or top) of the shear cell [39]. Including such friction according to Eq. (7), with the weight of the smaller disks $G^{(\mathrm{small})}=0.0036\ N$ and of the larger disks $G^{(\mathrm{large})}=0.005\ N$, should reduce the tangential velocities of the disks in the shear cell. From Fig. 8 we learn, that only a rather small value of the friction coefficient μ_{bottom} suffices to reduce the tangential velocities essentially. Thus, we are able to reach comparatively small tangential velocities [see profile for $\mu_{\mathrm{bottom}}=10^{-4}$ in Fig. 8] with the additional bottom friction. The system is thus much stronger influenced by the boundaries than by the details of the interaction model. In Fig. 9 we show the linear and logarithmic tangential velocity profiles for $\mu_{\mathrm{bottom}}=2\times10^{-5}$ which turned out to give the best agreement with the experiment.

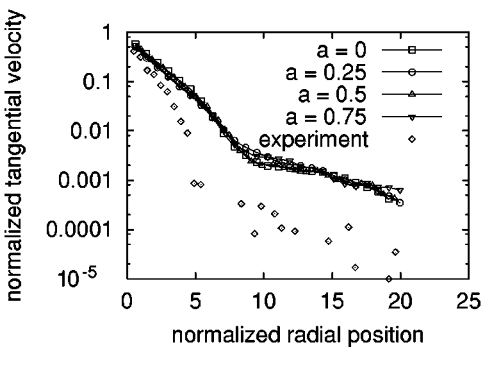

FIG. 7. Mean tangential velocity v_{t} versus radius $\underline{r}$ measured in a simulation using the friction law in Eq. ($\underline{5}$), with $\mu=0.44$ and different values of α compared with the experimental data.

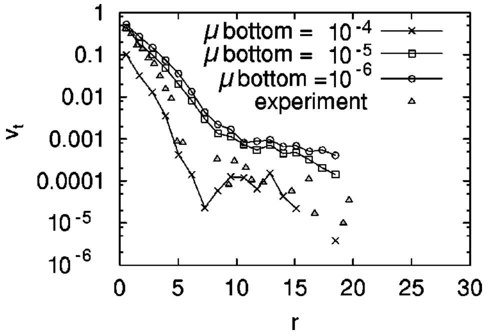

FIG. 8. Semilogarithmic plot of mean tangential velocity v_{t} vs radius $\underline{r}$ measured in a simulation with Coulomb friction between disks and bottom [see Eq. ($\underline{7}$)] for different friction coefficients μ_{bottom}.

For the following simulations we use the parameters from Table II and the Coulomb force from Eq. (4) between the disks and the bottom [see Eq. (7)] with $\mu_{\mathrm{bottom}}=2\times10^{-5}$. Also between the disks and the two cylindrical walls and between the disks themselves, we use Coulomb friction [see Eq. (4)] with a coefficient of friction $\mu=0.44$.

C. Rotations of the particles

The disks are free to rotate in our simulations. Besides the tangential velocities, also the spin s', i.e., the angular velocity of the disks, is of interest [see Fig. 10]. We obtain the mean spin in the same way as the tangential velocities and

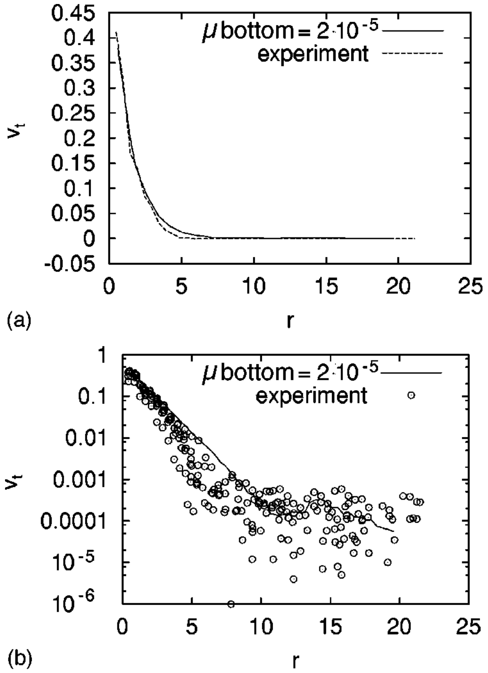

FIG. 9. Mean tangential velocity v_{t} versus radius $\underline{r}$ measured in a simulation with the parameters from Table $\underline{\mathrm{II}}$ friction and $\mu_{\mathrm{bottom}}=2\times10^{-5}$. (a) Linear plot. (b) Semilogarithmic plot. We plotted results from the experiment obtained with different rotational frequencies $\omega^{(\mathrm{in})}$ of the inner wheel to show the noise level in the ''static'' outer area.

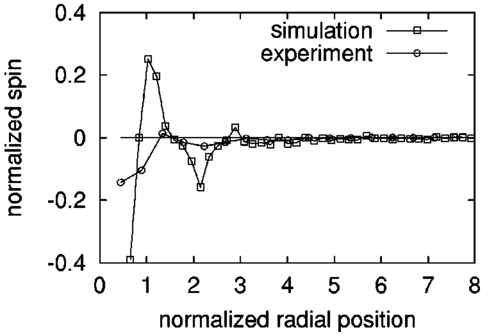

FIG. 10. Normalized mean spin s vs radius r.

use the normalized spin $s=(s' d^{(\mathrm{small})})/(\omega^{(\mathrm{in})} 2r^{(\mathrm{in})})$. Thus, $s=1$ means that a disk rolls over the inner wheel, and if $s<1$ there exists some sliding. Between the inner wheel and $r\approx 4$ the spin s oscillates between negative and positive values, i.e., the rotation sense of the disk changes and the magnitude decreases with increasing r. This result indicates that the disks are preferentially rolling over each other within the shear zone. Rolling necessarily requires that the rotation sense changes [see the sketch in Fig. 11]. Compared with the experiment, the absolute values of s are too high in the simulation. We attribute this to the fact that the friction with the bottom according to Eq. (7) only influences the translational motion of a disk but not its rotation.

The third kinematic quantity we look at is the radial velocity v_{r} of the disks. Due to the cylindrical boundaries the mean radial velocities obtained through the above described statistics must vanish, but still we can measure the fluctuations of the radial velocities. Therefore we take a closer look at the distribution of tangential, radial, and spin velocities v_{t}, v_{r}, and s of the disks. To quantify the distributions we use the root-mean-square (rms), defined as

$$\mathrm{rms}(x)=\sqrt{\langle (x-\langle x\rangle)^2\rangle}, \tag{8}$$

where $\langle\cdots\rangle$ denotes an average over time and a spatial average over a ring of radius r' and width Δr. Using the discrete probability distribution p_i for the n values x_i with $i=1,\ldots,n$, we can calculate the average $\langle\cdots\rangle$ in Eq. (8) to $\langle x\rangle=\sum_{i=1}^{n} x_i p_i$.

As an example, we show in Fig. 12 the rms for v_{t}. A steep decrease within the shear zone can be found, whereas the decrease more outside is much slower. Thus, the distributions of v_{t} are most broad near the inner wheel. This can be understood because the innermost area is most dynamic and the disks experience many collisions changing their tangential velocity. Compared with the experiment, the distributions within the shear zone are too narrow in the simulation. Let us remark that the rms of v_{r} and s show qualitatively the same behavior. The fluctuations of the tangential velocity are comparable to the v_{t} in the shear zone, but they are larger than v_{t} in the outer area.

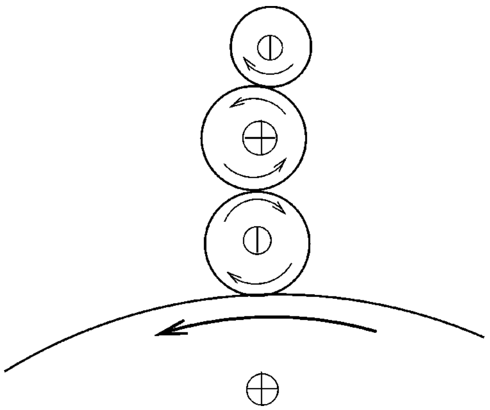

FIG. 11. Radially adjacent disks are rolling over each other.

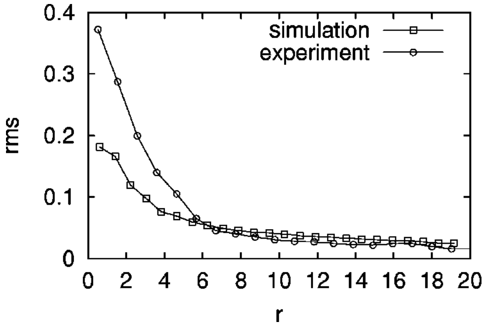

FIG. 12. Fluctuations of the tangential velocity distribution vs radius r.

In Fig. 13 we show distributions for v_{t} at three different rings of width $\Delta r=1/2$ and different radii $r=1$ (next to the shearing wheel), $r=4$ (near to the outer border of the shearing zone), and $r=10$ (in the static area). It can be seen that the distributions are becoming narrower with increasing r and that the averages of the distributions behave as described above. The semilogarithmic plots in Fig. 14 show that the distributions of all three quantities v_{t}, v_{r}, and s have exponentially decaying flanks at least for $r=4$ and $r=10$. This matches the experimental results qualitatively except for the distributions at $r=1$. Experimentally, a non-Gaussian but bimodal distribution is measured with two peaks at $v_{\mathrm{t}}=0$ and $v_{\mathrm{t}}\approx 0.6$ [26]. Thus a considerable amount of disks is at rest. Mainly some isolated disks without any contact with other disks contribute to these [40]. In simulations, a friction coefficient as small as $\mu_{\mathrm{bottom}}=2\times 10^{-5}$ is possibly too low to bring particles to a halt fast enough. Such a friction would have to act about 50 s to stop a disk with an initial velocity of 0.01 m/s, which is approximately the velocity of the inner ring of the shear cell and thus a realistic velocity for disks in the shear zone. Consequently, it is not surprising that we do

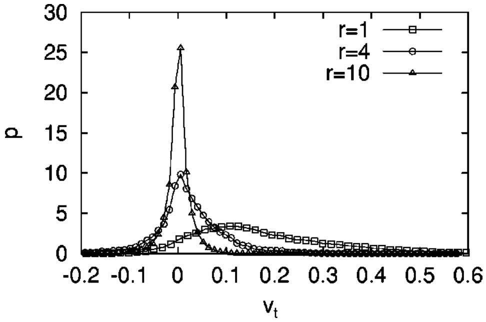

FIG. 13. Tangential velocity distribution for three different radii r. We plot the probability density p_{t} vs v_{t}. p_{t} fulfills the relation: $\int_{-\infty}^{+\infty} p_{\mathrm{t}}(v_{\mathrm{t}})dv_{\mathrm{t}}=1$.

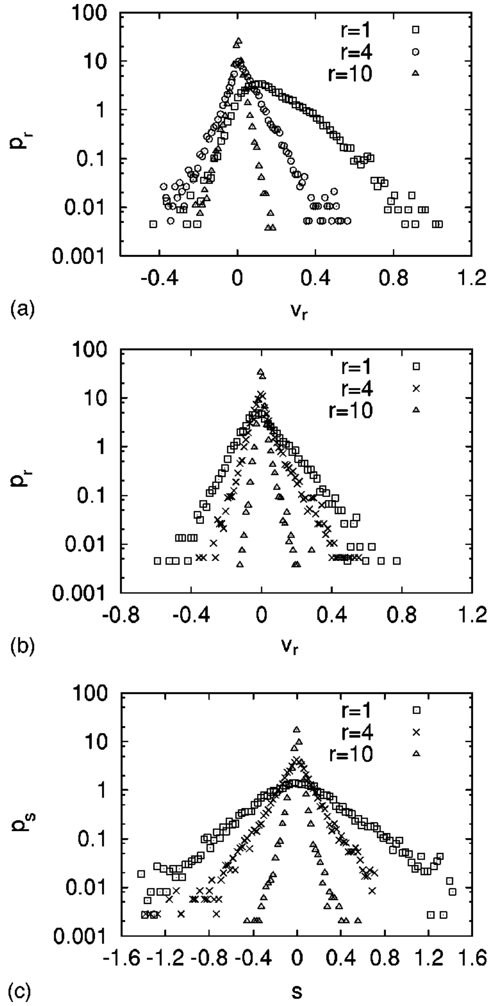

FIG. 14. Semilogarithmic plot of distributions for three different radii. (a) Distributions p_t of tangential velocities v_t. (b) Distributions p_r of radial velocities v_r. (c) Distributions p_s of spin velocities s.

not find in the simulation many disks at rest when using $\mu_{\mathrm{bottom}}=2\times10^{-5}$.

D. Variation of the volume fraction

Simulations with different volume fractions of the granulate also give different results. For the previous results we used $\rho=0.811$. In Fig. 15 we show that increasing the density by a certain amount ($\rho=0.824$) increases the velocities in the inner regions. With even higher densities ($\rho=0.834$) the system becomes blocked, it is too dense so that hardly any shearing takes place. Decreasing the volume fraction ($\rho=0.793$ and $\rho=0.784$) reduces the velocities. $\rho=0.793$ means that approximately the innermost layer of disks is removed, which should therefore be the lowest possible volume fraction for that motion of the disks that can be expected. Thus, with $\rho=0.784$ no shearing takes place. Consequently, a shearing of the granulate is possible only in a very small range of packing densities. In Fig. 16 we present spin velocity profiles for three different values of ρ. Increasing the density moves the first peak nearer to the inner shearing wheel. An influence of the packing density on the amplitude of the oscillations may also be expected because rotations of the disks are supposed to be increasingly frustrated by higher packing densities. On the other hand, the disks will not rotate at all if the packing density is too small and the disks are not in mutual contact.

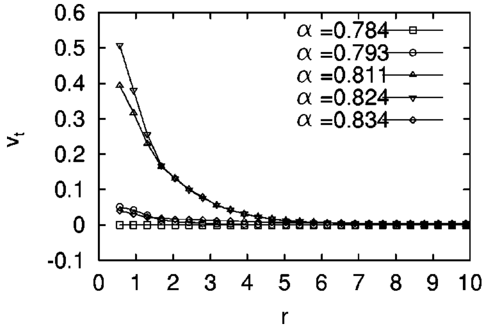

FIG. 15. Tangential velocity profiles for different volume fractions.

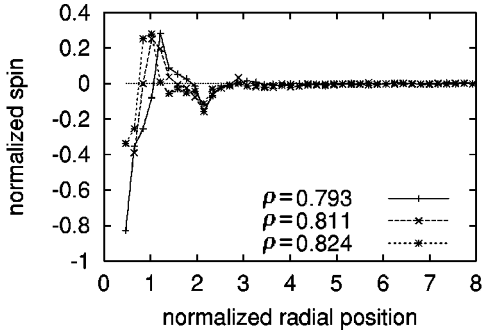

FIG. 16. Spin velocity profiles for three different volume fractions ρ.

In Fig. 17 the volume fraction of the disk packing at different radial positions in the shear cell is plotted. ρ shows distinct oscillations with a period of about one particle diameter in the shear zone and also close to the outer wall. These oscillations indicate that the disks are located in layers parallel to the wall within the shear zone. The density is lowest near the inner shearing wheel. This is reasonable because shearing is possible only in connection with dilatancy. The oscillations near the outer ring cannot be caused by the shearing but originate from the compression and the short range order induced by the outer ring. The solid line in Fig. 17 is an average of the oscillations and shows the dilatancy in the shear zone more clearly. Outside ρ is almost constant. This result is also obtained from the experiment.

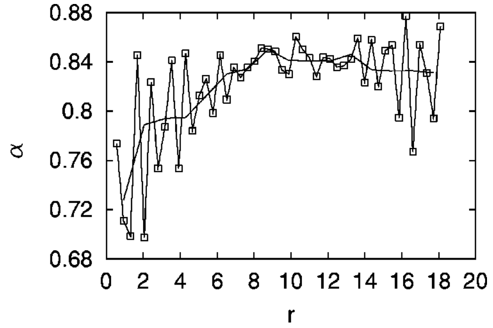

FIG. 17. Volume fraction ρ vs radial position r.

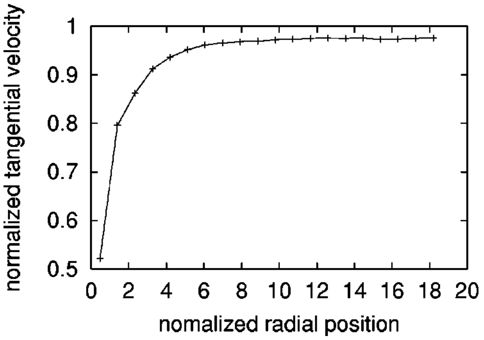

FIG. 18. Mean tangential velocity v_{t} vs radius $\underline{r}$ measured in a simulation with rotating outer wheel and immobile inner ring.

E. Inversion of the boundary condition

Now we present a simulation with rotating outer wheel and an immobile inner one [see Fig. 18 for the tangential velocities]. The situation with rotating outer wheel is very different from the one described above where the inner wheel rotated. Besides the disks within the innermost five disk radii, all disks follow the movement of the outer ring almost completely. This difference indicates that inertia effects can be important. It is clear that a disk tends to increase their radial position during shearing because of the centrifugal acceleration it experiences. In the case when the inner wheel rotates, the contact between the inner wheel and the disks is diminished due to this fact. In the case when the outer ring rotates, the disks are kept in good contact with the outer wheel and the disk packing follows its motion almost like a solid block.

V. CONTACTS AND FORCES

In this section, we focus on the contacts and contact forces within the packing of the disks. The contact network can easily be obtained by the simulation, whereas its reproduction from the experiment is difficult. Large contact forces are found along so-called force chains which can clearly been seen in Fig. 19. In some small areas, the initial triangular lattice remains frozen. Looking at a real-time movie of the simulation or at the experiment reveals that these force chains seem to have a certain mean direction depending on the rotation sense of the inner ring. A suitable quantity to measure the orientation of contacts is the fabric tensor

$$\underline{\underline{\alpha}}^{j}=\sum_{i=1}^{N}\underline{n}^{ji}\odot\underline{n}^{ji}, \qquad (9)$$

where $\underline{n}^{ij}$ denotes the unit vector of contact i of disk j and $\odot$ is the dyadic product. The sum in Eq. (9) runs over all contacts $i=1,\ldots,N$ of disk j so that a fabric tensor $\underline{\underline{\alpha}}^{j}$ for each disk j is defined. $\underline{\underline{\alpha}}^{j}$ is a symmetric second rank tensor and its principal axis (eigenvectors) can be calculated. The mean fabric tensors $\overline{\underline{\underline{\alpha}}^{j}}$ are obtained by averaging over $n^{\mathrm{t}}=1500$ snapshots taken at intervals of $\Delta t=0.2\mathrm{s}$ during 5 revolutions of the inner ring, starting after the first revolution. We use the parameters shown in Table II.

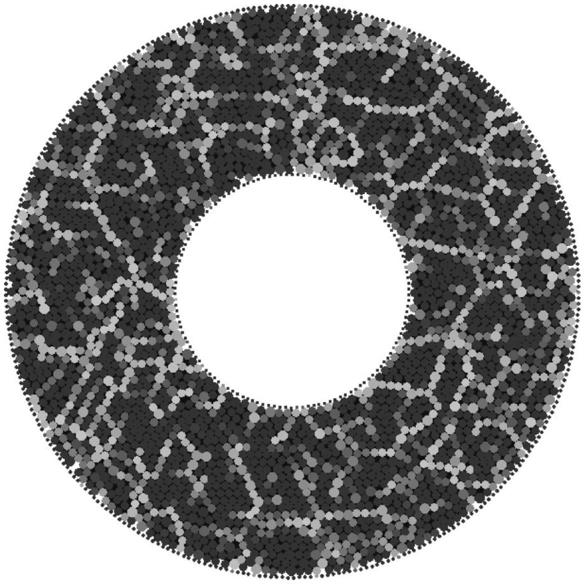

FIG. 19. Snapshot of simulation. The color indicates the normal stress acting on the disk: dark means low stress, light means high stress.

$\overline{\underline{\underline{\alpha}}^{j}}$ has different properties within the shear zone and outside. Relative to the radial direction, the orientation of $\overline{\underline{\underline{\alpha}}^{j}}$ is almost the same for all disks in the shear zone. For an essential fraction of the particles in the shear zone, the principal axis are tilted into the direction of the rotation of the inner ring [see Fig. 20(a)]. If the rotation sense of the inner ring changes, the principal axis are tilted into the opposite direction [see Fig. 20(d)]. Outside the shear zone, a peculiar structure can be seen; the orientation of $\overline{\underline{\underline{\alpha}}^{j}}$ differs from one disk to the next, meaning that the contact network outside the shear zone, built up during the first revolution, remains stable during the following shearing. For given velocity and rotation sense of the inner ring, this structure only depends on the spacing of the initial lattice, the distribution of the disks on the sites of the lattice, and their random, initial velocities. This observation is confirmed by a real-time movie of the simulation or the experiment. Since the time of examination is finite (e.g., five rotations) we are not able to observe very slow changes in the outer area.

A probability distribution of the orientation of the principal axis of the fabric tensors $\overline{\underline{\underline{\alpha}}^{j}}$ elucidates the described phenomena further in Fig. 20. Whereas it is difficult to extract this information from the experiment, a simulation is a comparatively easy and powerful tool for this task. Because of the rotational symmetry of the shear cell, we measure the orientation as the angle between the major principal axis and the radial direction. We define this angle as positive if the contact is tilted in mathematically positive direction, i.e., counterclockwise against the radial, outward direction. The following results were obtained by the same averaging procedure as described above. Figure 20 reveals distinct differences between the orientation of fabrics within different radial areas. In the shear zone [Figs. 20(a) and 20(d)], a triangular structure with preferred angles 90°, $-30°$, and $+30°$ is obvious. Furthermore, the angle $-30°$ is found more frequently than the angle $+30°$. Farther outside, the distribution is more homogenous [see Fig. 20(b)]. Near the outer ring, again a very distinct triangular structure occurs, but now, the peaks at $-30°$ and $+30°$ are equal. In Fig.

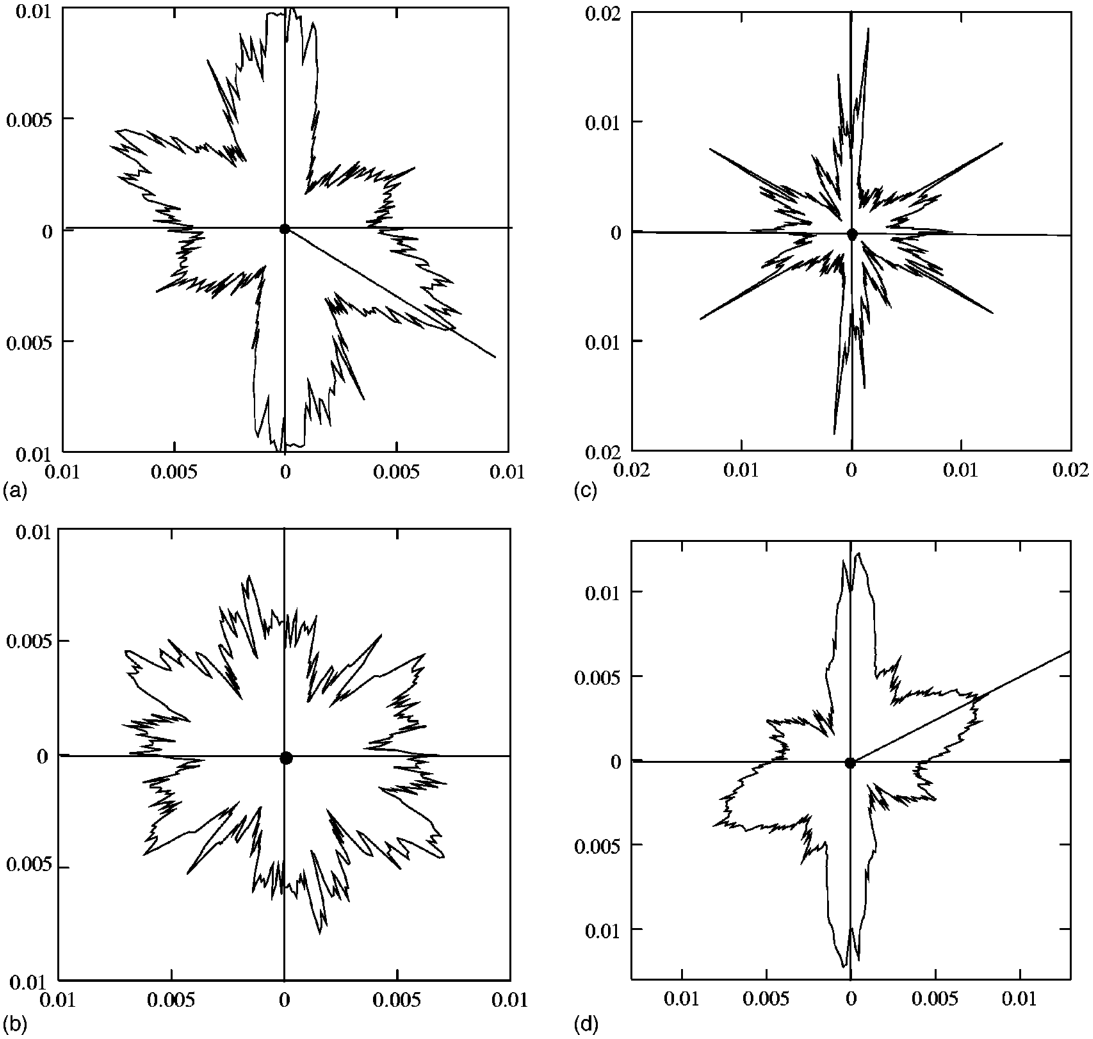

FIG. 20. Probability distributions of the orientation of the principal axis of the fabric tensor $\overline{\alpha^j}$ are shown in polar plots. They are measured in three different radial rings: (a) In the shear zone between $r=0$ and $r=6.6$, (b) between $r=6.6$ and $r=13.2$, and (c) between $r=13.2$ and $r=20$. The data in (d) are measured with an opposite rotation sense of the inner ring than in (a)–(c) with $0.0<r<6.6$ as in (a).

20(d) we present the data for an opposite rotation sense of the inner ring, to be compared to Fig. 20(a). We note that the peaks at $-30°$ and $+30°$ are exchanged with respect to their magnitude.

The angles 90°, $-30°$, and $+30°$ correspond to an annular triangular lattice or, in other words, the disks are located in annular layers. In the shear-zone [Figs. 20(a) and 20(d)], this structure is reasonable because it may allow sliding of the layers. A homogenous distribution outside the shear zone as in Fig. 20(b) is due to the missing influence of both dilation and geometrical order due to a wall. The repeated occurrence of the annular triangular lattice near the outer boundary cannot be ascribed to the shearing but is formed during the initial compression of the shear cell. If the rotation sense of the inner ring is changed, we get the same results as in Figs. 20(b) and 20(c). Only in the shear zone, more fabric tensors are oriented along $-30°$ than along $+30°$ [Fig. 20(d)] whereas in Fig. 20(a) we measured the opposite.

Note that the properties of the stress tensors (averaged over all contacts of one particle) have qualitatively the same properties as the fabric tensors. The major principal eigenvalue is preferentially tilted by 30° from the radial outward direction into the direction of rotation, and the distribution resembles a triangular network close to the walls.

Finally, we focus on the distribution of normal contact forces in sheared granulates. During the last years, this question became interesting mainly due to the so-called q model [41]. Also experimental [24,42] and numerical studies [43,44] examined the force distributions in static granular assemblies. Both experiment and simulation of the shear cell show force chains in the granulate during shearing which indicates that the contact force distribution is worth looking at. For the distribution $p(f/\langle f\rangle)$ of normalized contact forces $f/\langle f\rangle$ within a static granular material, the q model predicts an exponential decay for high forces and a power law for small forces. $\langle f\rangle$ is the average contact force and $p(f/\langle f\rangle)$ is normalized so that $\int_{-\infty}^{+\infty}p(x)dx=1$. In order to obtain the distribution of forces in the shear cell, we use 600 snapshots taken during one revolution of the inner ring and average over all disks. In Fig. 21 the results for the normal contact forces are shown. The distribution shows a distinct tail for high forces that can be fitted by an exponential function with an exponent between $-0.6f/\langle f\rangle$ and $-1.05f/\langle f\rangle$. The distribution becomes very noisy for small forces due to logarithmic binning and no clear statement is possible there.

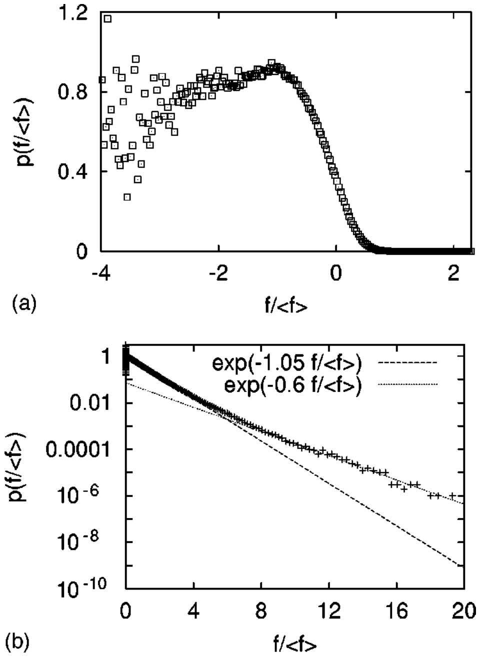

FIG. 21. (a) Distribution of normal contact forces $p(f/\langle f\rangle)$. (b) Semilogarithmic plot of the decrease for large normal contact forces.

VI. DISCUSSION AND OUTLOOK

It was shown that MD simulations are a suitable tool to reproduce the main features of granular shear flow in a Couette shear cell. We get quantitative agreement with the experiments, concerning the extent of the shear zone near the inner ring, the tangential velocity as function of the distance from the shearing wheel r, and the packing fraction, also as function of r. We achieve at least qualitative agreement when comparing the rotational velocities, the behavior of the velocity distributions, and the probabilities for large forces.

Predictions, concerning the orientation of the fabric tensor of the disks and the distribution of contact forces in the disk packing, have been made. For the first point, experimental results are very difficult to be obtained and are not accessible yet, and for the second point, reliable experimental results are possible for large forces only.

In general, simulations are a very powerful tool for at least two reasons. First, it is less difficult to change parameters in a simulation than in a real experiment, and second, some quantities are easily accessible from simulation but not from experiment. Thus, the simulation is useful to get more detailed insights, to make predictions, and to check experimental data-analysis methods.

The friction between disks and the bottom plate we used in the simulation causes further questions. Even when the agreement concerning the distribution of tangential velocities near the inner ring is reasonably reproduced by simulations, the rotational velocities are not damped by friction. Furthermore, we did not check how important inhomogeneities in the third dimension are. Especially the influence of the packing density and of the friction coefficient μ should be studied.

ACKNOWLEDGMENTS

The work presented here has been carried out in close cooperation with S. Luding and H.-J. Herrmann at the Institute for Computer Applications (ICA1). The experimental work we referred to was done by C. Veje from The Niels Bohr Institute in Copenhagen, Denmark, and D.W. Howell and R.P. Behringer from the Center for Nonlinear Science, Duke University in Durham.

---

[1] J. Van Cleef, Powder Technol. **79**, 304 (1991).

[2] H. M. Jaeger and S. R. Nagel, Science **255**, 1523 (1992).

[3] *Physics of Dry Granular Media,* edited by H. J. Herrmann, J.-P. Hovi, and S. Luding, Vol. 350 of *NATO Advanced Study Institute Series E: Applied Sciences* (Kluwer Academic, Dordrecht, 1998).

[4] *Powders & Grains 97,* edited by R. P. Behringer and J. T. Jenkins (Balkema, Rotterdam, 1997).

[5] *Behaviour of Granular Materials*, edited by B. Cambou (CISM, 1997).

[6] I. Vardoulakis and J. Sulem, *Bifurcation Analysis in Geomechanics* (Hapman & Hall, London, 1995).

[7] M. P. Allen and D. J. Tildesley, *Computer Simulation of Liquids* (Oxford University Press, Oxford, 1987).

[8] A. D. Rosato, K. J. Strandburg, F. Prinz, and R. H. Swendsen, Phys. Rev. Lett. **58**, 1038 (1987).

[9] S. Dippel and S. Luding, J. Phys. I **5**, 1527 (1995).

[10] T. Pöschel and H. J. Herrmann, Europhys. Lett. **29**, 123 (1995).

[11] S. Luding, E. Clément, A. Blumen, J. Rajchenbach, and J. Duran, Phys. Rev. E **50**, R1762 (1994).

[12] E. L. Grossman, Phys. Rev. E **56**, 3290 (1997).

[13] S. Luding, E. Clément, J. Rajchenbach, and J. Duran, Europhys. Lett. **36**, 247 (1996).

[14] T. Shinbrot, Nature (London) (London) **389**, 574 (1997).

[15] M. D. Shattuck, C. Bizon, P. B. Umbanhowar, J. B. Swift, and H. L. Swinney, in *Powders & Grains 97* (Ref. [4]), p. 345.

[16] C. S. Campbell and C. E. Brennen, J. Fluid Mech. **151**, 167 (1985).

[17] C. Thornton and C. W. Randall, in *Micromechanics of Granular Materials*, edited by Masao Satake (Elsevier, Amsterdam, 1988).

[18] Y. M. Bashir and J. D. Goddard, J. Rheol. **35**, 849 (1991).

[19] S. B. Savage, J. Fluid Mech. **241**, 109 (1992).

[20] J. F. Carr and D. M. Walker, Powder Technol. **1**, 369 (1967).

[21] Günter Löffelmann, Ph.D. thesis, Universität Fridericiana, Karlsruhe, 1989.

[22] H. Buggisch and G. Löffelmann (unpublished).

[23] B. Miller, C. O'Hern, and R. P. Behringer, Phys. Rev. Lett. **77**, 3110 (1996).

[24] D. Howell, B. Miller, C. O'Hern, and R. P. Behringer (unpublished).

[25] D. Howell and R. P. Behringer, in *Powders and Grains 97*, (Ref. [4]), p. 123.

[26] C. Veje, D. W. Howell, R. P. Behringer, S. Schöllmann, S. Luding, and H. Herrmann, in *Physics of Dry Granular Media* (Ref. [3]).

[27] P. A. Cundall and O. D. L. Strack, Géotechnique **29**, 47 (1979).

[28] H. G. Matuttis (unpublished).

[29] S. Dippel, Ph.D. thesis, Forschungszentrum, Jülich, 1998.

[30] J. Schäfer, S. Dippel, and D. E. Wolf, J. Phys. I **6**, 5 (1996).

[31] S. F. Foerster, M. Y. Louge, H. Chang, and K. Allia, Phys. Fluids **6**, 1108 (1994).

[32] L. Labous, A. D. Rosato, and R. Dave, Phys. Rev. E **56**, 5715 (1997).

[33] L. Brendel, in *Physics of Dry Granular Media* (Ref. [3]).

[34] S. Luding, M. Müller, and S. McNamara, in *The Validity of ''Molecular Chaos'' in Granular Flows*, World Congress on Particle Technology (Institution of Chemical Engineers, 1998).

[35] H. Hertz, J. für die reine u. angew. Math. **92**, 136 (1882).

[36] S. Roux, in *Physics of Dry Granular Media* (Ref. [3]).

[37] S. Luding and H.-G. Matuttis, in *Friction, Arching and Contact Dynamics*, edited by by D. E. Wolf and P. Grassberger (World Scientific, Singapore, 1997), pp. 207–211.

[38] G. A. Kohring, S. Melin, H. Puhl, H. J. Tillemans, and W. Vermöhlen, Comput. Methods Appl. Mech. Eng. **124**, 2273 (1995).

[39] C. Veje, D. Howell, and R. P. Behringer (private communication).

[40] C. Veje (private communication).

[41] S. N. Coppersmith, C.-h. Liu, S. Majumdar, O. Narayan, and T. A. Witten, Phys. Rev. E **53**, 4673 (1996).

[42] O. Tsoungui, D. Vallet, and J.-C. Charmet, Granular Matter **1**, 1 (1998).

[43] F. Radjai, D. Wolf, S. Roux, M. Jean, and J. J. Moreau, *Friction, Arching and Contact Dynamics*, edited by D. E. Wolf and P. Grassberger (World Scientific, Singapore, 1997).

[44] F. Radjai and D. E. Wolf, Granular Matter **1**, 1 (1998).